International Journal of Refractory Metals and Hard Materials 134 (2026) 107465

Contents lists available at ScienceDirect

International Journal of Refractory Metals and Hard Materials

journal homepage: www.elsevier.com/locate/IJRMHM

Diamond coating adhesion on WC – 6 %Co tools: A systematic study

A. Alatrash [a,*], D. Steinmüller-Nethl [b], H. Fitzek [a], S. Mitsche [a], D. Knez [a], M. Oberaigner [a], J. Arnold [b], A. Eckert [c], W. Grogger [a]

[a] Institute of Electron Microscopy and Nanoanalysis, Graz University of Technology and Center for Electron Microscopy, Steyrergasse 17, 8010 Graz, Austria
[b] CarbonCompetence GmbH, Weisstraße 9, 6112 Wattens, Austria
[c] G-ELIT Präzisionswerkzeug GmbH, Lengeder Straße 29 – 35, D – 13407 Berlin, Germany

ARTICLE INFO

Keywords:
Diamond
Coating
Adhesion
Microscopy
Magnetic saturation
EBSD

ABSTRACT

Achieving a consistent and well-adhering diamond coating remains a challenge for WC-Co tools. We analyze the microstructure of tungsten carbide and cobalt using electron microscopy and diffraction techniques. We examine batches with good and poor layer adhesion at three stages: uncoated, after pretreatment, and after coating. The samples are differentiated based on their magnetic saturation value. This study focuses on WC-6 %Co with a mean WC grain size of 1.2 μm and vanadium doping.

The results reveal a direct correlation between magnetic saturation and diamond coating adhesion to the substrate surface. Magnetic values represent the tungsten content and, consequently, the corrosion resistance of the binder phase (cobalt). An ignoble binder (low corrosion resistance) is prone to excessive etching and improper diamond nucleation. Batches with a noble binder show consistent coating formation, consistent diameter reduction, and consistent depletion zone depth. In contrast, batches with an ignoble binder exhibit significant changes in these areas.

1. Introduction

Tungsten carbide is a well-established and essential material among hard metals. This unique material combines high hardness and wear resistance using a two-phase system [1–3]. The most common system used is WC mixed with cobalt as a binder phase. Tungsten carbide has a hexagonal close-packed crystal structure; cobalt has two crystal structures, face-centered cubic (fcc) and hexagonal close-packed (hcp). Cobalt is hcp at room temperature, and fcc is the high-temperature stable phase. The grain size has a direct effect on the tool properties; a fine grain size results in higher hardness [4]. One common method of limiting WC grain size is to use growth inhibitors, such as chromium or vanadium, during the sintering process. These inhibitors are typically used at low percentages (<1 %). he binder phase also plays a significant role in influencing tool properties. Increasing the binder phase amount results in higher transverse rupture strength, whereas a lower amount provides higher hardness [2,5]. This soft binder phase also causes ductile failure [6].

Many applications require diamond coatings to extend the life of work tools and provide greater hardness and wear resistance. The strength of the layer bonding, and thus the adhesion of the coating layer, depends crucially on how well carbon can diffuse and nucleate in the surface of the work tool. During the pretreatment process, increasing the diffusion depth can cause inconsistent carbon growth and create an intermediate layer between the nucleation zones and the coating. In other words, inhomogeneous growth results in drastic alterations to the coating's mechanical properties. [7]. Research on WC-Co coatings mainly concerns tribological properties, performance, and tool longevity. Before material testing, it is crucial to understand how the WC-Co system works and how the coating layer interacts with the substrate. The goal then becomes producing a reliable coating consistently. For the diamond coating to adhere to the surface, the cobalt must be etched from the outermost layers of the work tool (less than 10 μm) to allow the diamond to nucleate and form the coating from the inside of the sample up to 5–20 μm on its surface. Optimal depletion zones range from 4 μm. If the zones are too large, however, the carbide becomes brittle and the diamond layer, firmly attached to the carbide surface, dissolves with it. Problems with the coating often arise from the deposited diamond within the sample [7]. This region is referred to as a buffer zone or depletion layer. Coating problems result in delamination, which is an adhesive fracture that originates in the depletion layer between the substrate and the coating layer. [6]. Tahir et al. [6] modeled

* Corresponding author.
E-mail address: anas.alatrash@felmi-zfe.at (A. Alatrash).

https://doi.org/10.1016/j.ijrmhm.2025.107465
Received 6 August 2025; Received in revised form 16 September 2025; Accepted 27 September 2025
Available online 29 September 2025

the adhesion strength of coatings on a substrate surface and claimed that a higher substrate surface roughness provides better coating adhesion.

Carbide is a common material for industrial cutting tools and dominates the global market with a 60 % share [8]. Carbides have high abrasion resistance and fracture toughness, allowing for a wide range of applications in high-performance machines. While carbide owes its hardness to tungsten carbide (WC), sufficient toughness for many applications is only guaranteed by the binder. The binder is usually cobalt (Co), but it can also be nickel (Ni), iron (Fe), or nickel-chromium (NiCr). The binder holds the WC grains together in the material structure. Diamond coating significantly increases the wear resistance of the tool (increasing tool life by between three and 25 times) due to its special hardness.

To be able to deposit diamonds on carbides, the binder material must be 'passivated' on the surface. As cobalt is used as the main binder material, the focus in this description is on Co. Co catalytically converts the sp^3-hybridised carbon (diamond) into sp^2-hybridised carbon (graphite) as shown in Fig. 1.

The formation of this graphitic layer significantly impairs the adhesion of the coating. To solve this problem, the cobalt (or the other binders) must be passivated. Passivation of the cobalt can be achieved by two methods:

1. Wet chemical etching: Removal of the cobalt from the uppermost layers of the carbide.
2. Intermediate: An Intermediate layer system that is applied to the cemented carbide and can withstand a subsequent diamond coating in an atomic hydrogen atmosphere at approximately 850 °C.

Quality control in the production of tungsten carbide takes place after sintering, when the magnetic saturation is measured. Each company has specific tolerances for its materials based on the substances' chemical compositions. To understand the effect of magnetic saturation, one must have a critical understanding of the W-C-Co phase diagram. This system has been studied and simulated in several studies [3,9,10]. The carbon window for WC/Co systems is of the utmost importance. Carbon-poor alloys exhibit η-phase formation, while samples with excessive carbon content result in graphite formation within the WC-Co matrix [11]. The effect of carbon variation has also been reported by [12]. Systems with relatively low carbon wt% result in higher tungsten dissolution in cobalt, resulting in relatively low magnetic saturation. Conversely, systems with relatively high carbon wt% result in lower tungsten dissolution in cobalt, resulting in relatively high magnetic saturation.

The specific composition of a hard metal significantly affects the diamond coating process and how well the diamond layer adheres to the substrate. To ensure a reliable diamond coating, the substrate material must be analyzed and the chemical pretreatment adjusted. In some cases, this must be done for different batches of the same carbide grade. One common characteristic measure of hard metals is magnetic saturation. Furthermore, we demonstrate its dramatic importance in ensuring the success of the diamond coating step in the case of WC-Co.

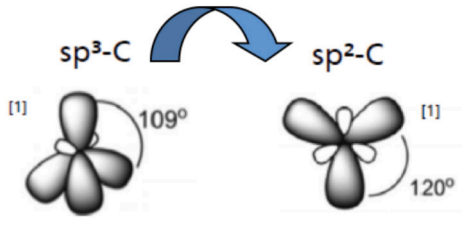

Fig. 1. Illustration of conversion of sp3-hybridised carbon to sp2-hybridised carbon.

2. Theory

To understand the material and its behavior, understanding the composite physical properties is the starting point. Cobalt is a ferromagnetic material, and measuring the magnetic properties is the most common measurement technique for tools using cobalt as a binder phase. The magnetic saturation gives direct information about tungsten dissolution in Co. Roebuck et al. [3] give Eq. (1) to calculate the magnetic saturation of Co-W in the WC-Co system from the amount of W present in the binder, where σ is the magnetic saturation of Co-W alloy and σ_0 is the magnetic saturation of pure cobalt. $4\pi\sigma_0$ is taken to be $202^* 10^{-7} \left(\frac{\mu Tm^3}{kg}\right)$ as reported in [3]. The binder relative magnetic saturation (BRM) is given in Eq. (2) and is expressed as a percentage of the work tool value to pure cobalt [13].

Eq. (1): Magnetic saturation of Co-W alloy in WC-Co

$$4\pi\sigma = 4\pi\left(\sigma_0 - 8\, m_w{}^*10^{-7}\right)\# \tag{1}$$

Eq. (2): Calculation of binder's relative magnetic saturation

$$BRM\% = \frac{\sigma}{\sigma_o}{}^*100\# \tag{2}$$

Konyashin et al. [12] explain the root cause for a varying magnetic saturation in tungsten carbide, and how the carbon content plays a role in the dissolution of tungsten in cobalt. In that regard, tungsten may dissolve in cobalt up to 8 wt% [3], this helps WC-Co in the densification process during sintering. For a stable mixture of 10 wt% Cobalt, a carbon content between 5.4 and 5.55 wt% is a must; this percentage increases with the decrease in cobalt wt%.

The amount of tungsten dissolved and cobalt present in the binder phase directly relates to the change in cobalt's lattice parameter. According to [3], the change in the lattice parameter with respect to tungsten and carbon contents is given by the following equation,

Eq. (3): Calculation of cobalt lattice parameter with respect to tungsten and cobalt content

$$a^{fcc} = a_0^{ffc} + 0.00036m_w + 0.0012m_c\# \tag{3}$$

where a_0^{ffc} is the lattice parameter of pure cobalt and is equal to 0.3548 nm, m_w is the atomic concentration of tungsten, and m_c is carbon present in the hard metal.

The binder phase in hard metals is present in both the hexagonal close-packed (hcp) and face-centered cubic (fcc) modifications. Roebuck et al. [3] have observed an exclusive formation of fcc cobalt with tungsten concentrations greater than 5.9 at.%. This resulted in samples having low BRM values. However, this interpretation of hcp-fcc ratios is unreliable because the role of sample preparation is not considered. Preparation plays a vital role in the quality of surface analysis. Winriaski et al. [14] provide an excellent insight into the role of preparation. We report the implications of using common preparation methods and their impact on cobalt characterizationin [15]. Studies concerned with hcp-fcc distribution also look into the role of grain size [13,16]; however, we do not report any influence on the grain size in our measurements, as we find no correlation for our research question.

Cobalt metal has an hcp structure below 450 °C, at higher temperatures, fcc is the stable crystallographic phase. As a binder, dissolved W can stabilize the fcc phase down to room temperature, and consequently, improve the corrosion resistance [17]. Typically, in a WC-Co hard metal, the Co alloy will be a mixture of mostly fcc and partially hcp. The distribution of different elements and phases is measured using Electron Backscatter Diffraction (EBSD). For cobalt data, the amount of hcp present in our samples is reported as a percentage of hcp of total cobalt (rHCP) and is calculated as follows:

Eq. (4): Calculating relative hcp fraction

$$rHCP(\%) = \frac{Co_{hcp}}{Co_{hcp} + Co_{fcc}} * 100\# \quad (4)$$

3. Experimental

The samples were investigated in batches at three different stages of production: blank, pretreated, and coated. All samples are of the same grade and chemical composition (WC-6 %Co, vanadium-doped, with an average grain size of 1.2 μm) and were produced by G-Elit-Präzisionswerkzeug-GmbH under the name DK120.

Magnetic saturation measurements were carried out at G-Elit usinga Foerster's KOERZIMAT 1.097. As shown in Table 1 our samples have BRM values between 79 % and 98 %. Samples with BRM values above 90 % are referred to as HMS (highly magnetic saturated), while those below 90 % are referred to as LMS (low magnetic saturated).

Table 1 displays all the samples characterized in this work. The first column contains the batch number and sample type. X indicates an uncoated sample, V indicates a pre-treated sample, and B indicates a coated sample. If numbers appear in the first cell, it means that this exact sample was investigated in two different states. Next is the sample number followed by the relative magnetic saturation of the binder to pure cobalt.

All samples underwent the same preparation and characterization route for electron microscopy analysis. Samples were prepared as cross-sections and milled using the broad ion beam milling technique with a Gatan Ilion Model 693 Precision Cross-Section Mill [18]. Phase mapping and characterization were carried out using electron backscatter diffraction (EBSD) in a scanning electron microscope (SEM). The device used was a Zeiss Ultra 55 with an EDAX Trident detector. EBSD measurements were performed with a beam energy of 15 kV and 7.2 nA, 10 × 10 binning of the Thorlabs scientific, high-resolution EBSD camera, and an integration time of 7–8 ms. The EBSD characterization area was confined to a 60 × 50 μm window with a step size of 0.05 μm.

Surface quality plays an integral role in cobalt indexing, as even slight imperfections can result in significant shifts in cobalt phase analysis. Additionally, poor focus can result in misrepresentation of the sample. These aspects must always be considered when measuring and evaluating EBSD data. Fig. 2 shows an example of coated samples and their phase maps generated in OIM software using EBSD data. It illustrates the difference in depletion zone thickness and the phase distribution of the different elements in an HMS and an LMS sample.

Table 1
Overview of all samples investigated and the corresponding BRM.

Batch No.	Sample No.	BRM (%)	Batch No.	Sample No.	BRM (%)
7390×	5	93.89	8377× 8377B	4	83.33
7390×	15	95.63	8377B	5	84.16
7390×	16	95.79	7472×	1	81.68
7390 V	E	94.64	7472× 7472B	2	80.86
7390× 7390B	F	94.64	7472× 7472B	3	81.68
N7390B	2	97.36	7472× 7472B	4	81.68
N7390B	3	96.53	6915×	7	85.07
N7390B	4	98.18	6915×	13	83.00
N7390×	5	96.53	6915×	14	82.67
B7390B	1	98.18	6915 V	B	83.75
B7390B	2	96.53	6915× 6915B	C	83.75
B7390B	3	97.36	0348× 0348B	14	88.28
B7390B	4	95.71	0348 V	51	–
B7390B	5	96.53	1439×	1	80.86
8377B	1	84.98	1439 V	1	79.21
8377× 8377B	2	84.98	1439B	14	83.33
8377B	3	84.98			

The XRD measurements are obtained using a Siemens D5005 powder X-ray diffractometer. The powders for X-ray Powder Diffraction (XRPD) were meticulously compressed into pellets and subsequently characterized. Samples for Co lattice parameter measurements were prepared using standard metallurgical preparation. All XRD measurements were conducted at ambient temperature. The XRPD measurement parameters are as follows: an 8-s dwell time and a 0.02° step size, and a 50-s dwell time and a 0.02° step size for Co measurements.

The strength of layer adhesion is determined through the implementation of a sandblasting test, employing the Wasserman's CEMAT-2 II apparatus. The duration for which the coating maintains its integrity on the surface is utilized as a metric for the assessment of adhesion strength. The adhesion tests have been performed using the following materials and parameters: Corundum particles (F90, 150 μm grain size), initial pressure at 3 bar, and the subsequent pressure at 5 bar, at 10 mm distance from the nozzle.

A calibration was conducted on diamond-coated tools, and the coating adhesion was categorized as excellent to poor over the duration of the coating's resilience to the blasting test.

The microscope employed for TEM experiments is the Austrian Scanning Transmission Electron Microscope (ASTEM) FEI Titan^3 G2 60–300 operated at 300 kV. A variety of samples were prepared for the purpose of TEM lamellae production, with the process being carried out using a FIB-SEM Dual Beam Microscope (FEI NOVA200). The analysis was conducted in STEM mode, employing camera lengths ranging from 85 to 95 mm.

4. Results

4.1. Base powder analysis

In order to ascertain the underlying cause of the deviation observed in diamond-coated tools, it is necessary to begin the analysis with raw cobalt powders. These cobalts are utilized by the tool manufacturer interchangeably. The objective of this study is to identify any discrepancies that may have a bearing on the manufacturing of WC-Co tools. In light of the aforementioned information, an investigation is warranted into the phase distribution of the powders in question. This investigation is intended to ascertain whether the observed variation in rHCP across the batches can be justified. Three standard cobalt powders were investigated; these were simply named Powder 1, 2, and 3.

XRD measurements were utilized to discern potential variations in the hcp/fcc content of the powders. As Illustrated in Fig. 3, the hcp Co peaks are denoted by red circles, while the fcc Co peaks are indicated by blue triangles. As illustrated in Fig. 3, the analyzed powders exhibit a high degree of similarity, with no statistically significant differences in the amount of hcp and fcc Co. Cobalt powder predominantly exhibits hexagonal close-packed (hcp) crystal structure in its raw powder form. However, in the context of hard metals, the predominant form is fcc. Correlating and quantifying cobalt in its two modifications in two different processes is challenging due to the significant difference in hcp/fcc distribution. In summary, the measurements obtained demonstrate an absence of correlation between the selection of distinct powders and the resulting final product. Consequently, we proceed with the production chain to investigate further influencing parameters.

4.2. Uncoated samples

The initial investigative phase entailed a comprehensive characterization of the binder phase [19], employing EBSD as the investigative approach was formulated. The investigative focus centered on the hcp-fcc ratio in Co and its eventual influence on the reliability of diamond coating adhesion on the work tool. Preliminary analyses were conducted on uncoated specimens.

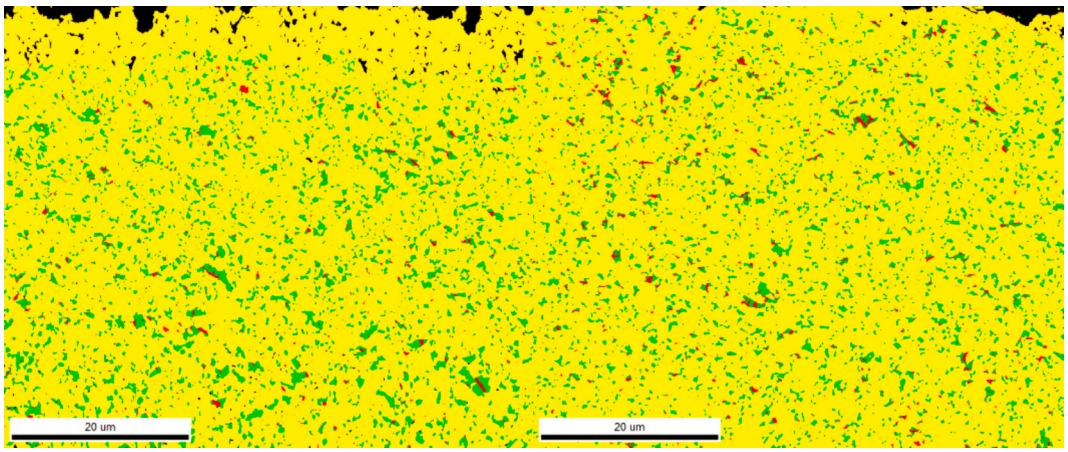

Fig. 2. Images of phase maps generated using EBSD of coated samples. Left: HMS sample (7390B_F), right: LMS sample (7472B_3). Colour code: red: hcp Cobalt; green: fcc Cobalt; yellow: Tungsten Carbide; black: no signal. Scans were done at the edge of the samples. (For interpretation of the references to colour in this figure legend, the reader is referred to the web version of this article.)

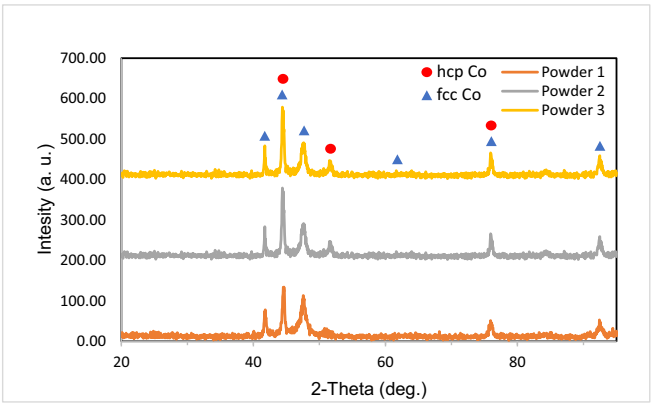

Fig. 3. Plot of XRD signal of three cobalt powders and peak intesities corresponding to hcp Co and fcc Co crystal structures.

4.2.1. *Surface & phase analysis*

Surface imaging was conducted using SE and AsB detectors for the majority of the samples. However, the surfaces of the uncoated samples appeared identical to their counterparts due to the absence of any additional processing. However, the scope was subsequently constrained to EBSD characterization. These EBSD analyses were conducted to ascertain the relationship between rHCP and BRM.

In Fig. 4 and Fig. 5, we present surface images captured through the use of the SE detector for two samples, as depicted in the left column. The right column presents the corresponding EBSD phase distribution of the samples. The legend indicates the total fraction, which is the number of indexed points corresponding to each element and phase out of all available points. The partition fraction indicates the percentage of each element and phase concerning valid indexed points. Points that have a value of 0 are not considered. The objective of this study is to ascertain the crystal phase distribution of Co. A discernible discrepancy in the proportion of rHCP Co is evident in Table 2, with values of 1.7 % and 8 % for LMS and HMS, respectively. This indicates that 1.7 % of the Co in the sample exhibits the hcp structure, while the remaining 8 % manifests as fcc. This finding corresponds to our expectations: In a sample exhibiting high magnetic saturation, a negligible amount of W is dissolved in the Co. Therefore, the fcc structure exhibits reduced stability, resulting in an increased proportion of hcp (the stable form at room temperature).

In Table 2, we list the characterized uncoated samples with the corresponding BRM, total cobalt indexed using EBSD, and the rHCP are reported. The results are plotted as a function of rHCP with respect to BRM in Fig. 6, to visualize the data and check if there is any correlation between the parameters.

From Fig. 6, samples characterized by increased BRM frequently exhibit elevated rHCP levels, while those with diminished BRM often demonstrate reduced rHCP values, as highlighted with the trendline. However, this finding is inconsistent, prompting further investigation into the mechanisms underlying this variation, particularly concerning the role of magnetic saturation. Notwithstanding, these investigations

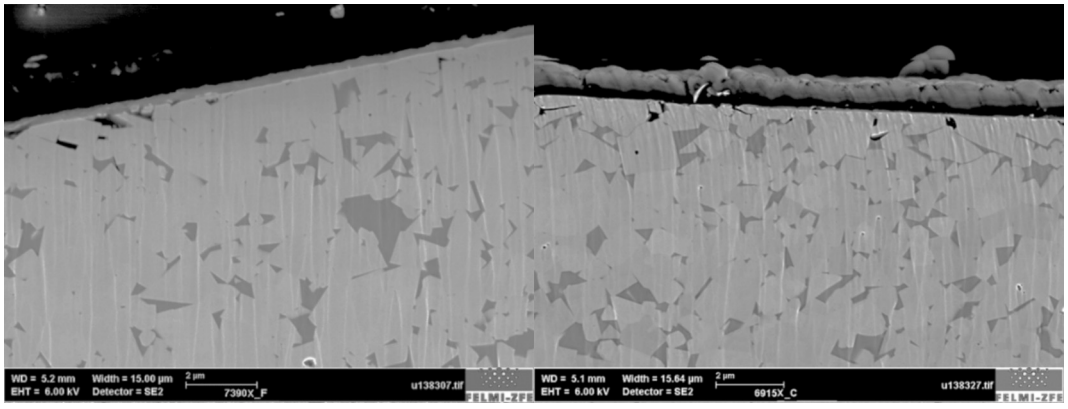

Fig. 4. SEM images of a cross section surface of uncoated WC-Co edge of an HMS (Left, sample: 7390×_F) and an LMS (right, sample: 6915×_C), imaged using SE in SEM. Images show the surface morphology before any processing.

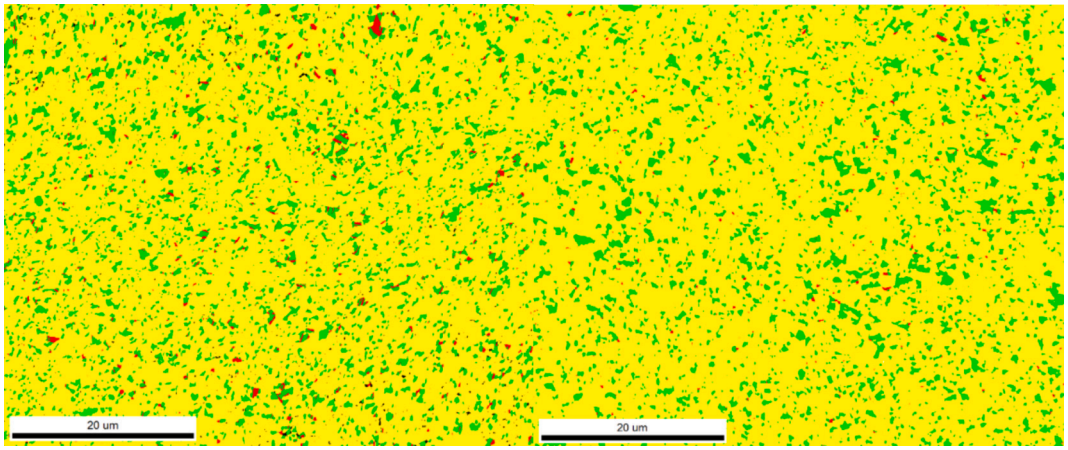

Fig. 5. Images of phase maps generated using EBSD of uncoated samples. Left: HMS sample (7390×_F), right: LMS sample (6915×_C).Colour code: red: hcp Cobalt; green: fcc Cobalt; yellow: Tungsten Carbide; black: no signal. Scans were done in the bulk of the samples. (For interpretation of the references to colour in this figure legend, the reader is referred to the web version of this article.)

Table 2
Summary of cobalt phase analysis of selected uncoated samples with the corresponding BRM and rHCP values.

Batch No.	Sample No.	BRM (%)	Total Co (%)	rHCP (%)	Batch No.	Sample No.	BRM (%)	Total Co (%)	rHCP (%)
7390×	15	95.63	8.7	10.3	7472×	4	81.68	12	5.83
7390×	16	95.79	13.6	11.0	6915×	13	83.00	13.1	3.05
7390×	F	94.64	13.7	8.03	6915×	14	82.67	12.8	3.12
8377×	2	84.98	12.9	3.88	6915×	C	83.75	11.7	1.71
8377×	4	83.33	12.2	4.91	0348×	14	88.28	10.1	0.99
7472×	2	80.86	13.1	6.11	1439×	1	80.86	8.10	8.62
7472×	3	81.68	12.1	6.61					

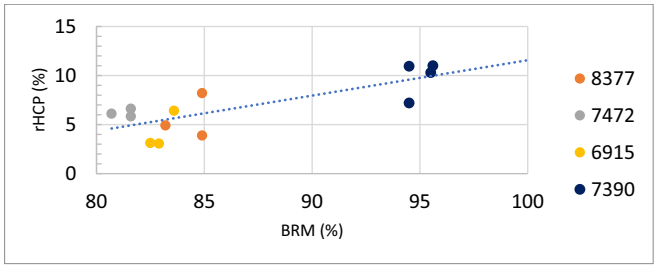

Fig. 6. Visualizing the distribution of rHCP of uncoated samples with respect to BRM. rHCP was calculated from EBSD data with respect to total cobalt. A dotted-trendline highlights the correlation between the increase in rHCP and BRM. Each point represents a sample and a measurement point. Samples are grouped based on their batch number.

form the foundation for the comparison with pretreated and coated samples.

4.2.2. *Nanostructure analysis*

To confirm that this scenario is indeed what we are facing, we use energy dispersive x-ray spectroscopy (EDX) in the transmission electron microscope (TEM). We look at the line scan of the tungsten signal within a cobalt subgain, as shown in Fig. 7, and compare the values from different samples.

Fig. 7 (left) presents an electron diffraction (EDX) map of tungsten in the WC-Co specimen, as observed in a transmission electron microscope (TEM). The objective of this study is to ascertain the extent of tungsten dissolution in cobalt. To this end, a line scan is conducted within the binder phase. The W-L signal was subsequently quantified to determine the percentage of W present, as illustrated in Fig. 7 (right). This procedure is implemented to provide empirical evidence in support of the theoretical framework outlined by [3,12].

In Fig. 8, we demonstrate a comparison between W wt% concentration measured in cobalt subgrain of a select LMS and HMS samples. Our measurements substantiate the discrepancy in dissolved tungsten within the cobalt grains. Samples represented by blue lines correspond to HMS samples, which exhibit the lowest tungsten content in the binder phase. This phenomenon, as elucidated in [12,16] and stated in [20], is hypothesized to be attributable to the disparity in carbon wt% present within the samples. An elevated level of carbon results in a diminished propensity for tungsten to infiltrate the cobalt binder. Consequently, the magnetic moment of cobalt approaches its theoretical value, thereby yielding a high BRM. The diffusion mechanism of tungsten in cobalt can be discerned by observing the cobalt channels.

Fig. 9 illustrates the use of high-angle annular dark field imaging (HAADF) in STEM mode, revealing the presence of bright points that are concentrated within a dark matrix. In this mode, the brightness of an atom is directly proportional to its mass. Bright atoms, therefore, are analogous to tungsten, while dark atoms are analogous to cobalt. This is a critical aspect for comprehending the alterations in magnetic saturation. The presence of diffused atoms and tungsten clusters in the alloy serves to diminish the magnetic moment of cobalt. In addition, this observation corroborates the findings reported in [3,12,13]. It can be concluded that an increase in the dissolution of tungsten results in a decrease in the BRM. Furthermore, the monitoring of the change in lattice parameter resulting from the dissolution of tungsten in cobalt is possible through XRD analysis.

In Table 3, the array of measured samples encompasses both uncoated and coated specimens. The inclusion of coated samples is predicated on the assumption that the magnetic saturation change subsequent to coating is negligible. Assuming this to be true, the XRD measurements are independent of the investigation stage.

In Fig. 10 the XRD results are depicted based on the lattice constant values that were obtained with respect to the BRM value. Each batch is distinguished by a unique colour, with samples within each batch

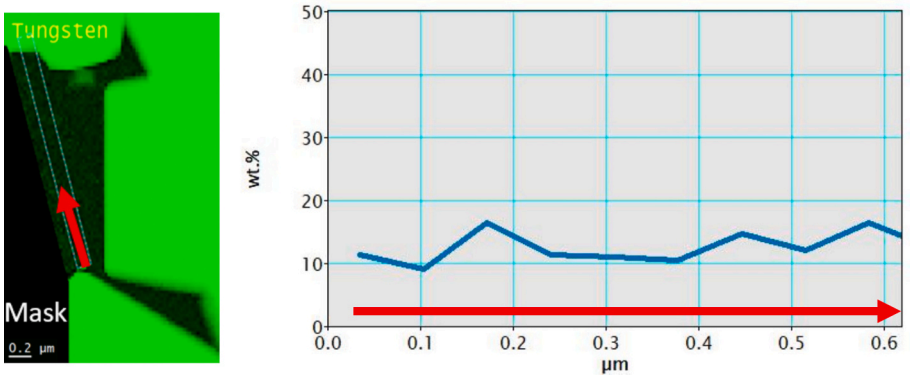

Fig. 7. Left: EDX map of W of an uncoated LMS sample (6915×_14), generated in DigitalMicrograph using STEM-EDX, with a red arrow marking the location and direction of the line scan. Right: a blue line showing the W in wt% in cobalt subgain, and a red arrow corresponding to the plotting direction. (For interpretation of the references to colour in this figure legend, the reader is referred to the web version of this article.)

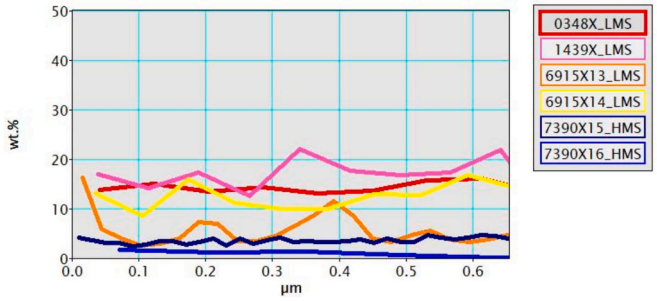

Fig. 8. Comparison of the W wt% concentration in Co for all investigated WC-Co TEM uncoated samples generated in DigitalMicrograph using STEM-EDX data.

sharing the same colour. The figure indicates that all HMS samples exhibit values of 0.3564 nm or below, while all NMS samples demonstrate values of at least 0.3565 nm or above. These values exceed the Co theoretical lattice constant value, which is commonly accepted as 0.3544 nm. However, a discernible variation in the lattice constant of cobalt is observed, contingent on the degree of magnetic saturation. This assertion is further substantiated by the findings reported in [3]. This interaction is driven by the corrosion mechanism between WC and Co, where fcc Co is stabilized by the dissolution of WC [21,22]. Consequently, an increase in the dissolution of tungsten should result in an elevated lattice constant. In the event of the dissolution of a minimal quantity of tungsten, the calculated value of the lattice constant will approximate the theoretical value. As demonstrated in Fig. 10, this hypothesis is supported by the measurement data.

4.3. Pretreatment analysis

The pretreatment procedure is the process most relevant to coating companies. Should any issues emerge during the coating process, they are most frequently identified during this stage. The samples undergo a series of treatments and preparations prior to the coating process. This process involves wet chemical etching of the cobalt from the surface and ultrasonic seeding with a nano diamond particle solution (average 5 nm), thereby facilitating the initiation of diamond growth centers. The coating procedure is executed through the implementation of hot-filament chemical vapor deposition (HF-CVD). The focal point of this investigation lies in the reduction of diameter, a consequence of wet chemical etching, surface morphology, and the depletion zone that emerges subsequent to pretreatment.

4.3.1. Diameter reduction

The samples were measured at CarbonCompetence before and after

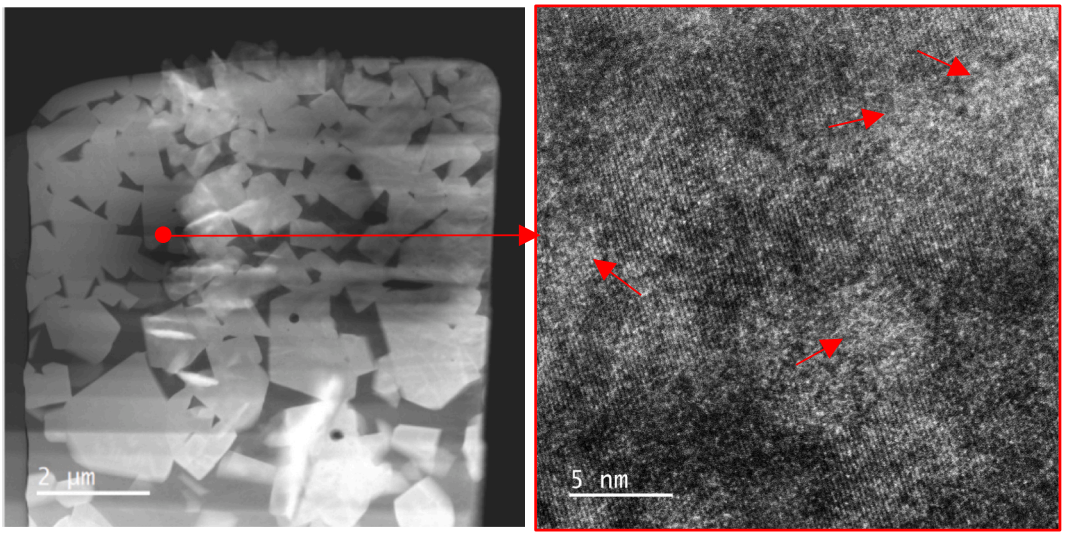

Fig. 9. Left: an overview image of an uncoated LMS sample (0348×_1) taken in HAADF-STEM mode. Right: A zoomed-in image of the marked cobalt grain showing tungsten clusters in cobalt taken in HAADFT-STEM mode.

Table 3
Measured samples using XRD with the corresponding BRM and lattice parameter value.

Batch No.	Sample No.	BRM (%)	Lattice parameter (nm)	Batch No.	Sample No.	BRM (%)	Lattice parameter (nm)
7390×	5	93.89	0.3563	8377B	3	84.98	0.3565
7390×	15	95.63	0.3556	8377B	4	83.33	0.3570
N7390×	1	95.71	0.3562	8377B	5	84.16	0.3570
N7390B	2	97.36	0.3560	7472B	2	80.86	0.3569
N7390B	4	98.18	0.3564	7472B	4	81.68	0.3570
B7390B	3	97.36	0.3563	6915×	7	85.07	0.3568
B7390B	5	96.53	0.3561	6915×	14	82.67	0.3565
8377B	2	84.98	0.3568				

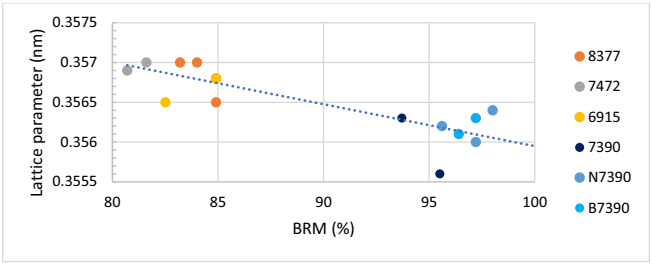

Fig. 10. Plot of lattice constant values, measured using XRD, of different batches with respect to BRM. Plot contains coated and uncoated samples, as the variation in lattice parameter after coating is assumed to be negligible. A dotted-trendline highlights the correlation between the increase in BRM and the decrease in lattice parameter. Each point represents a sample and a measurement point. Samples are grouped based on their batch number. Points in same colour are samples in the sample batch. Points in shades of blue originate from the same production batch, but were coated and received at different stages of the project. (For interpretation of the references to colour in this figure legend, the reader is referred to the web version of this article.)

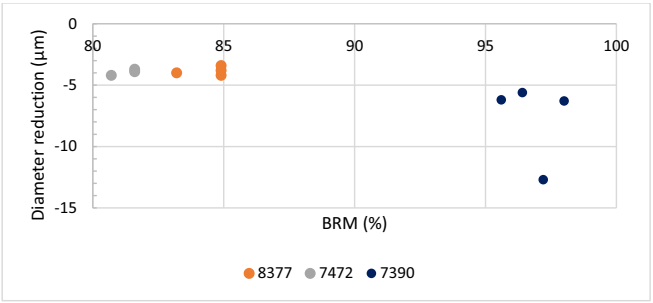

Fig. 11. Plot of diameter reduction data or pretreated samples, measured using a laser micrometer, with respect to BRM. Each point represents a sample and a measurement point. Samples are grouped based on their batch number.

the pretreatment process using the laser micrometer XLS40 from AEROEL. At FELMI-ZFE, surface morphology and depletion zone characterization are conducted using a SEM ZEISS Ultra 55.

In Table 4, the batch and sample numbers are delineated in the initial two columns, respectively. The relative magnetic saturation is enumerated in column 3, while the change in diameter, measured at a distance of 10 mm from the edge of the sample, is detailed in column 4. The alteration is the disparity between the thickness subsequent to pretreatment, which is calculated by subtracting the pretreatment thickness from the initial thickness (prior to the pretreatment process). The procedure is employed to ascertain the material's response to the etching process. The pretreatment procedure was consistent for all processed samples. It has been observed that samples with elevated BRM values undergo more extensive etching. This phenomenon can be attributed to the variation in the dissolved tungsten content present in the cobalt binder. The presence of tungsten has been shown to stabilize the binder phase, thereby reducing its susceptibility to excessive etching [16,17].

The data presented in Table 4 has been plotted in Fig. 11. The degree of etching appears to be directly proportional to the extent of magnetic saturation. HMS samples demonstrate inconsistent etching and greater material loss in comparison to LMS batches. This phenomenon can be attributed to the varying presence rates of tungsten within the cobalt binder. Tungsten has been demonstrated to enhance the stability of cobalt and augment its corrosion resistance. Consequently, the elevated presence of tungsten in the binder engenders a more stable and noble cobalt, and vice versa [12,17].

4.3.2. *Surface analysis*

Surface morphology and depletion zone characterization are done using Zeiss Ultra 55 at 6 kV acceleration voltage using the SE2 detector. In Fig. 12, a comparison is presented between the edge of WC-Co tools, with LMS positioned on the left and HMS on the right. The objective of surface analysis is to ascertain the impact of pretreatment on the surface of the specimen, as this surface will serve as the intermediate layer for the diamond coating that will be applied subsequently.

A visual inspection of the surface morphology in Fig. 12 reveals a pronounced difference between the samples. The LMS sample displays a shallow depletion zone with relatively straight edges, while the HMS sample exhibits a deeper depletion layer and a crumbling edge. This finding aligns with the overarching theme that emerged in the preceding section. The binder phase is excessively etched, causing WC grains to crumble and consequently lose more material.

4.4. *Coating measurements*

Coating companies frequently possess a set of recipes for diverse materials and compositions. However, to ensure consistent outcomes, a process of optimization is often necessary. In the event that the coating

Table 4
Measured reduction in diameter after wet chemical etching process.

Batch No.	Sample No.	BRM (%)	Diameter reduction (µm)	Batch No.	Sample No.	BRM (%)	Diameter reduction (µm)
N7390	1	95.6	−6.2	8377	3	84.9	−3.8
N7390	2	97.2	−12.7	8377	4	83.2	−4
N7390	3	96.4	−5.6	7472	2	80.7	−3.9
N7390	4	98	−6.3	7472	3	81.6	−4.2
8377	1	84.9	−3.4	7472	4	88.1	−3.7
8377	2	84.9	−4.2				

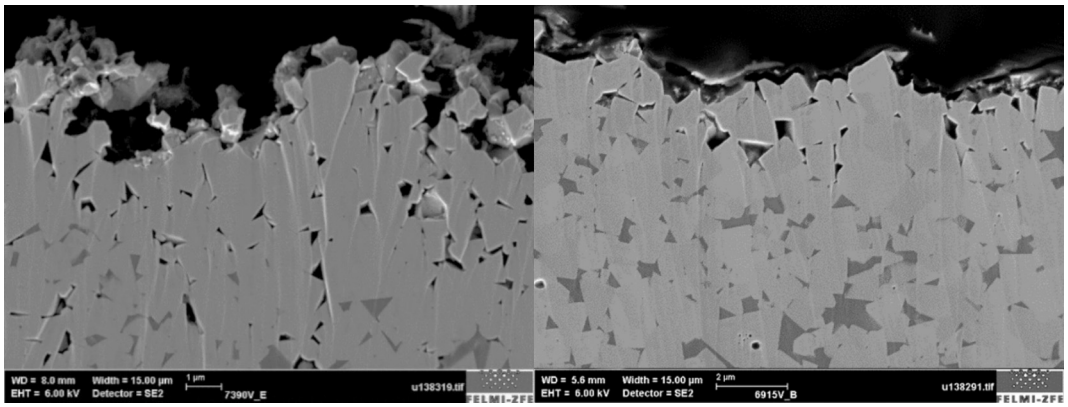

Fig. 12. SEM images of a cross section surface of pretreated WC-Co edge of an HMS (Left, Sample: 7390 V_E) and an LMS (right, Sample: 6915 V_B) samples, imaged using SE in SEM. Images show the surface morphology and the depth of depletion zone. Areas in the substrate with very dark contrast are depleted cobalt binder.

layer is not applied in accordance with the prescribed protocol, the resultant coating may exhibit defects such as irregular growth, voids, or embrittlement [7]. To that end, we employ Raman spectroscopy and TEM to investigate and characterize the properties of the coating layer from the surface up to the deepest point in the depletion zone. All coated samples underwent the same coating procedure and recipe at Carbon-Competence GmbH. The application of a nano-crystalline diamond coating with a thickness of approximately 7 µm was carried out.

4.4.1. Blasting test

The diameter reduction observed following pretreatment indicates that HMS samples are susceptible to significant material losses. Furthermore, the outcomes of the blasting test demonstrate that etching the HMS carbide results in the formation of a substantial, brittle depletion zone (devoid of Co). Consequently, a significant amount of carbide is removed, leading to a substantial reduction in diameter.

This results in an increase in remaining cobalt in the area proximate to the interface, which, in turn, has a deleterious effect on diamond growth (sp^2 formation) and results in inadequate coating adhesion.

The results of the blasting test are presented in Table 5, we show the results of the blasting test. The number, given in seconds, in column 4 represents how much the coating withstood colloidal silica blasting. The purpose of this test is to evaluate the adhesion of the diamond coating on WC-Co. A higher number indicates strong adhesion to the substrate, while a lower number indicates weak adhesion. The results of this study are presented in. The strength of coating adhesion is determined by the duration for which it maintains its integrity. The adhesion strength is evaluated as follows::

- 0–60 s: bad adhesion
- 60–90 s: good adhesion
- 90–120 s: very good adhesion
- 120+ seconds: excellent adhesion

In Fig. 13, the distribution of layer adhesion strength is contingent upon BRM. The results of the HMS samples exhibited significant variability, with adhesion strength ranging from all adhesion ratings, with the majority of the points falling within the poor adhesion category. Conversely, all LMS samples exhibited exemplary layer adhesion. This substantial discrepancy can be ascribed to the pretreatment procedure, wherein HMS samples underwent a significantly more pronounced etching, resulting in the surface of the hard metal becoming more brittle and less stable. This, in turn, led to a reduction in corrosion resistance.

4.4.2. Depletion zone

As previously demonstrated in Fig. 13. a clear distinction in morphology is evident between LMS and HMS. LMS samples exhibited signs of cobalt etching, while HMS samples demonstrated a more pronounced etching pattern. In addition, Figure 13demonstrates inconsistent layer adhesion strength. Subsequent investigation of the depletion zone will be undertaken to ascertain a potential correlation between the depth of the zone and the adhesion strength. As previously elucidated, the aforementioned zone is the area in which cobalt is etched from the surface. These etched areas serve as the foundation for the diamond

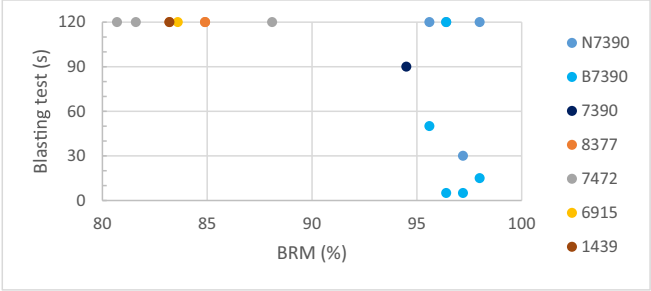

Fig. 13. Strength of coating adhesion of coated samples, given in blasting test duration (s), plotted with respect to BRM. Samples are grouped based on their batch number.

Table 5
Blasting test results for several coated WC-Co samples with the corresponding BRM values.

Batch No.	Sample No.	BRM (%)	Blasting test (s)	Batch No.	Sample No.	BRM (%)	Blasting test (s)
N7390	1	95.6	120+	7390	F	94.5	90
N7390	2	97.2	30	8377	2	84.9	120+
N7390	3	96.4	120+	8377	3	84.9	120+
N7390	4	98	120+	8377	4	83.2	120+
B7390	1	98	15	7472	2	80.7	120+
B7390	2	96.4	5	7472	3	81.6	120+
B7390	3	97.2	5	7472	4	88.1	120+
B7390	4	95.6	50	6915	C	83.6	120+
B7390	5	96.4	120+	1439	14	83.2	120+

coating. The dissolution of cobalt in WC-Co has been demonstrated to be influenced by the grain size and the amount of cobalt present [17,23]. However, it is particularly intriguing to explore the potential of magnetic saturation as an influencing parameter on cobalt dissolution.

To illustrate the methodology employed in the measurement of depletion zones, refer to Fig. 14. Given that the edge of the specimen is not a straight line but rather a curve, due to the geometry of the specimen and the etching process, a reference measurement line was established slightly within the surface to account for this deviation. The second line is set where it intersects with at least depleted grains, as illustrated. According to the findings of the study, the rough estimate of the error in thickness measurement is assumed to be ±0.5 μm, as a result of edge morphology. This estimation is regarded as conservative, as the edge morphology of LMS samples is characterized by "smoothness."

In Table 6, we show the results of depletion zone measurements; the measurements of pretreated samples are added to this part. The results are plotted in Fig. 15.

Looking at Fig. 15, the excessive etching of cobalt is apparent. The thickness of the depletion zone is approximately 3.5 ± 0.5 μm for LMS samples. However, the thickness of HMS samples exceeds 13 ± 0.5 μm, which is approximately four times the thickness of LMS for an equivalent duration of etching. It has been determined that, in addition to the grain size and cobalt content, the stability of the cobalt binder is a critical factor in the substrate preparation process for diamond coating.

4.4.3. Diamond coating: analysis of interface region

The present study examines the carbon formation from deep within the depletion zone up to the surface. Cobalt is etched to create a space for diamond to nucleate and bind to WC grains. The strength of the carbon bonding to the surface is a determining factor in the adhesion strength of the coating. The purpose of Raman measurement is to identify the type of carbon nucleating, as it allows for the identification of carbon hybridization. The following text is intended to provide a comprehensive overview of the subject matter.

Using this information, we are interested in differentiating between the diverse types of carbon present in the samples, as carbon can be found in sp^2 and sp^3 hybridization. The hybridization of carbon in graphite is sp^2 and it is sp^3 hybridised in diamond. The samples are characterized based on the depth of the characterized pore and the width of the G-band (Γ_G). The G-band is typical for sp^2 hybridised carbon, more specifically, graphene-type structures. As is generally the case in Raman spectroscopy, the width of the band is a measure of the crystallinity of the sample, with narrow bands denoting a high degree of crystallinity and broad band denoting a low degree of crystallinity, meaning an amorphous sample [24]. There are further indications of the degree of crystallinity and defects in graphitic/ amorphous carbon type samples that have been studied over the years, such as the G-band position or the D-band (1350 cm^{-1})/G-band intensity ratio [25]. However, in this case, the straightforward width of the G-band is used as it is a more robust measure of crystallinity and less subject to influences such as mechanical strain or precursor dependents. The Raman spectra are fitted with the Breit-Wigner-Fano (BWF) intensity formula (G-band) and a Lorentz-profile (D-band) as stated in [26] and Γ_G is calculated. For the experiments, several pores were randomly selected throughout the depletion zone of each sample. We noticed the absence of the diamond peak at 1332 cm^{-1}. This means that it is not diamond that is formed in the depletion zone, but rather graphite. For that reason, we compared the samples based on the width of the G-band at 1583 cm^{-1} and the depth of each pore. Under our assumption, the sharper the band, the more crystalline the carbon in the pore is.

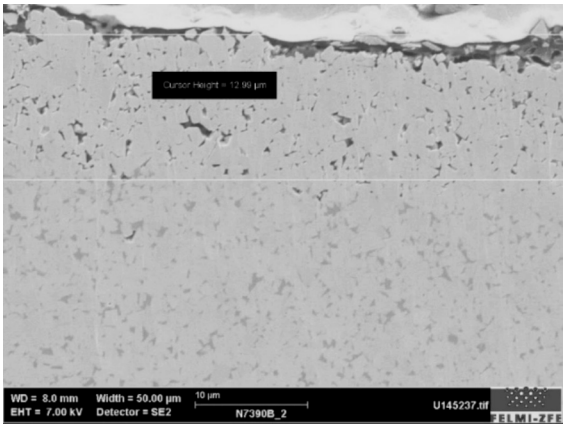

Fig. 14. SEM image of a coated HMS sample (N7390B_2) cross section, imaged using SE in SEM. The image is used to illustrate depletion zone thickness measurement procedure.

Fig. 16 shows an example fitting of the Breit-Wigner-Fano (BWF) intensity formula. The fitting procedure is done according to [26]. The blue points are the individual measurement points acquired. The width of the G-band (Γg) is calculated from the BWF formula. For the experiments, several pores were randomly selected throughout the depletion zone of each sample. We noticed the absence of the diamond peak at 1332 cm^{-1}. This means that it is not diamond that is formed in the depletion zone, but rather graphite. For that reason, we compared the samples based on the width of the G-band at 1583 cm^{-1} and the depth of each pore. The peak width gives information about structural disorder, a narrow peak suggests an ordered crystalline order, whereas a broad peak indicates an increased defects and/or crystalline disorder. The D-band indicates the degree of structural order or size of graphite domains, though this peak does not exist in perfect graphene. The sharpness of both D- and G-bands is associated with the size of graphite domains. Amorphous carbon also exhibits the characteristic of showing D- and G-bands, though the peaks are broader [24,27].

In Fig. 17, we showcase the Raman measurement points and how the depth of the pore is measured. A reference is set at the outer surface of the substrate, and the distance between the reference surface and the pore is the pore depth measurement shown in Fig. 18.

In Fig. 18, the samples are plotted with respect to Γg (width of G-band) and depth (how far the characterized pore is from the substrate surface, not counting the coating). The HMS samples are plotted with blue squares, meanwhile the LMS samples are plotted in red triangles. The aim is to find a correlation between the type of carbon formation and magnetic saturation or pore depth. We found that, in most cases, the formation of the coating starts as graphite (until roughly 45–55 cm^{-1}, where the peak width indicates the transition from nanocrystalline graphite to amorphous carbon occurs; the carbon formation below 45 cm^{-1} peak width is considered graphite).

Nevertheless, the carbon signal of both formations was detected throughout the depletion zone. Adding to that, a clear difference is present, 18 out of 35 measured signals (roughly 51 %) for LMS samples are below the 50 cm^{-1} thresholds, whereas only 3 out of 50 measurement points (6 %) lie below this line for HMS samples. This means there is indeed a preference for a form of graphite in the LMS samples, and the carbon formation in HMS samples tends to be amorphous carbon. This could explain the drastic diameter of these samples; although both carbon modifications are known to be very brittle, the amorphous carbon present does not seem to bond properly in cobalt-depleted pores; further studies are required to understand why and how this happens.

In addition, to illustrate the difference between the Raman signal and the change in carbon structure, 3 points from an LMS (Fig. 19) and 3 points from an HMS (Fig. 20) are plotted, and these points are marked with a black border in Fig. 18. The three-point measurements are a result of the three regions shown in Fig. 18 The following are observed: Below the line, where we get a sharp G-band; InLine: inside the transition region marked with red, where we see G-band broadening; and AboveLine: where the Raman signal is broad and corresponds to amorphous carbon. From these figures, we can distinguish the difference in crystallinity and Raman signal. The presence of amorphous carbon raises a new

Table 6
Results of SEM characterization data of depletion zone thickness with respect to BRM.

Batch No.	Sample No.	BRM (%)	Depletion zone (μm)	Batch No.	Sample No.	BRM (%)	Depletion zone (μm)
N7390B	2	97.2	13.0	7472B	2	80.7	3.42
N7390B	4	98	9.72	7472B	3	81.6	3.03
B7390B	2	96.4	14.0	6915 V	B	83.6	2.97
7390 V	E	94.5	7.39	6915B	C	83.6	2.88
7390B	F	94.5	7.48	0348B	14	88.28	1.78
8377B	2	84.9	3.20	1439 V	49	79.1	2.18
8377B	3	84.9	4.30	1439B	1	83.2	1.98

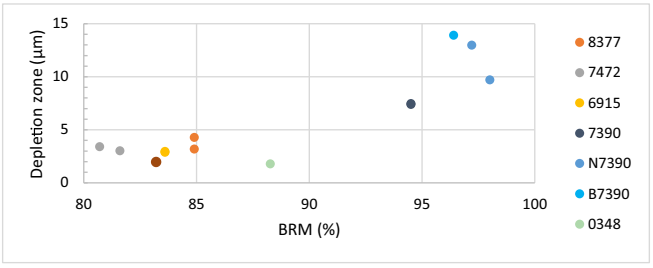

Fig. 15. Plot of distribution of depletion zone thickness of coated samples, measured in SEM using cross section cuts, with respect to BRM. Samples are grouped based on their batch number.

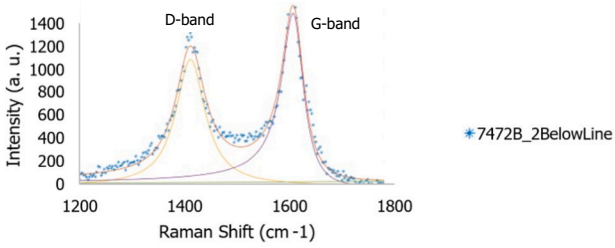

Fig. 16. Intesity of Raman signal of a pore in a coated sample (7472B_2), plotted in blue stars, and the corresponding BWF equation fitting lines. The fitting is used to calculate the width of the G-band (Γg). (For interpretation of the references to colour in this figure legend, the reader is referred to the web version of this article.)

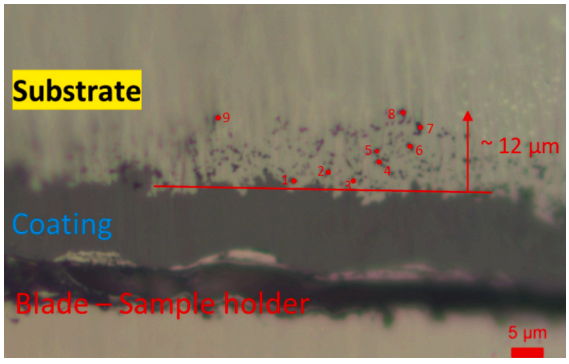

Fig. 17. A light microscope image of an analyzed cross section of an HMS sample (N7390B_4), showing an overview image of the sample holder, coating and substrate, the locations of Raman measurements and depletion zone thickness from reference line.

clarification for delaminating diamond coating, as amorphous carbon is typically more brittle than graphite [28]. This means that, because of excessive cobalt etching, diamond seeds are unable to diffuse through the depletion zone and form nucleation zones, causing amorphous

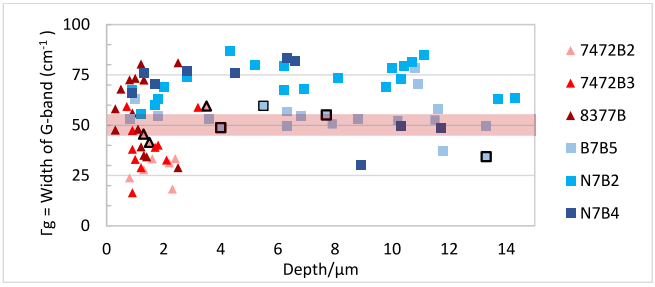

Fig. 18. Plot of average G-band width versus pore depth of selected coated samples. Average G-band width is calculated by fitting Raman signal using BWF approximation. Pore depth is the distance of the pore from the substrate of the surface, measured using a light microscope. Samples are grouped based on their batch number. Points in same colour resemble the same sample. Samples with similar colour and same plot shape have similar BRM value. Colour code: HMS samples: blue squares. LMS: red triangles. Red line: the transition zone from graphite (below line) to amorphous carbon (above line). (For interpretation of the references to colour in this figure legend, the reader is referred to the web version of this article.)

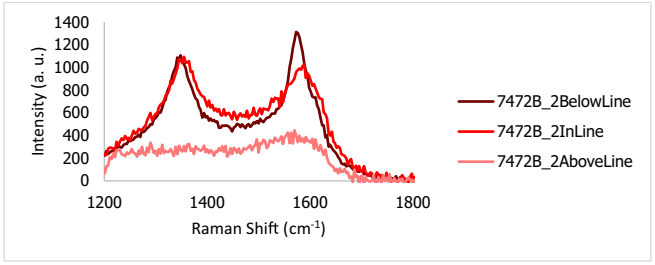

Fig. 19. Raman signal of three measurement points in the depletion zone of a coated LMS sample (7472B_2), illustrating the difference in G-band peak width carbon signal. The plotted points are the black-outlined triangles, of the sample (7472B_2), of the three defined graph regions in Fig. 18.

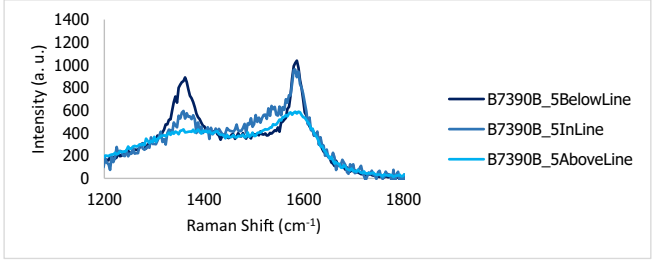

Fig. 20. Plot of the Raman signal of three measurement points in the depletion zone of a coated HMS sample (B7390B_5), illustrating the difference in G-band peak width carbon signal. The plotted points are the black-outlined squared, of the sample B7390B_5, of the three defined graph regions in Fig. 18.

carbon growth.

Furthermore, we investigate the coating layer on two samples, an HMS (blue) and an LMS (red) sample, as shown in Fig. 21. The Raman shift is almost identical; from this, we conclude that the difference in layer adhesion originates from the differences in the depletion zone. This cements our assumption: the problem in layer adhesion is not a flaw of the coating but rather related to different outcomes after the pre-treatment process. For materials to be suitable for diamond coating of WC-6 %Co composition with vanadium doping, the magnetic saturation must be strictly controlled. Batches with BRM above 90 % do not seem reliable substrates for diamond coating.

Building on the Raman measurements, we opt to do EDX and EELS in TEM for two reasons: to investigate the difference in cobalt pores (check if there is cobalt residue) and to investigate the carbon structure in the depletion zone, complementing the Raman experiments described above. Carbon diffuses through the surface, starts nucleation, and works its way up to the surface, then forms a diamond coating. To see this, we observe the fine-structure of core-loss edges, in EELS, which is called Electron Loss Near-Edge Structure (ELNES) [29,30].

The EELS spectrum shown in Fig. 22 are taken from LMS (left) and HMS (right) samples. These maps show the location of carbon and the corresponding modification. We chose to highlight the ELNES signal between 285 and 305 eV to cover the σ* and π* of Carbon K edges. Comparing the near-edge structure of the C-K ionization edge with data from [31], there are three carbon modifications that can be present: Diamond, graphite, and amorphous carbon. Diamond has a σ* peak at around 292 eV. Graphite and amorphous carbon have a characteristic π* at 285 eV. Amorphous carbon has however a broad σ* signal, which is the signal obtained from our samples in Fig. 22. It was only possible to monitor the carbon structure in LMS, as it was not possible to extract a sufficient signal from HMS samples. The signal obtained from our samples in Fig. 22 (left), and is identical to what has been observed in [32,33]. It was only possible to monitor the carbon structure in LMS, as it was not possible to extract a sufficient signal from HMS samples. This agrees with our observation of amorphous carbon in the LMS samples.

4.4.4. *Surface & phase analysis*

The characterization procedure for coated samples using SEM with SE2 and EBSD was identical to the surface and phase analysis. In a manner consistent with prior surface characterization, a comparison was made between the morphology and rHCP to BRM of these samples.

Fig. 23 shows a comparison between the surface morphology of a coated HMS (7390B_F) and a coated LMS (7472B_3) samples; Fig. 24 shows the phase maps generated using EBSD. The features of the variation of magnetic saturation and its effect on sample quality are immediate. We illustrate the fragmentation and crumbling of the substrate. We can also see fractured WC grains present within the diamond coating itself in HMS. The LMS sample shows an inconspicuous cross-section of the surface.

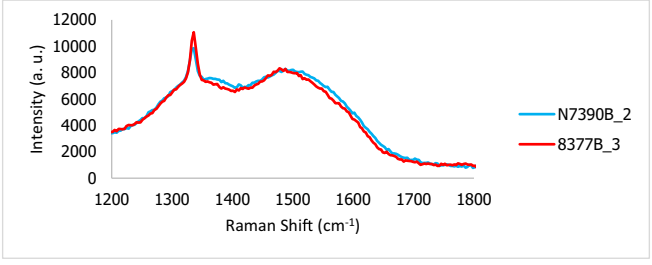

Fig. 21. Plot of the Raman signal of the diamond coating of a coated LMS (red, sample 8377B_3) and HMS (blue, sample N7390B_2) samples, showing the characteristics diamond peak at 1332 cm^{-1}. (For interpretation of the references to colour in this figure legend, the reader is referred to the web version of this article.)

Finally, EBSD analysis is done for all coated samples available, and rHCP results are reported in Table 7. We compare the results obtained in Table 7 for coated samples to the results shown in Table 2 for uncoated samples and plot them in Fig. 25.

For the sake of clarity and comparison, batches are not distinguished, but rather categorized based on BRM, as illustrated in Fig. 22. An intriguing trend has been observed: for HMS, a decrease in rHCP is evident following the application of diamond coating. Conversely, for LMS samples, the trend is inverse; rHCP levels exhibited an increase subsequent to the coating process. The decline in HMS samples could be attributed to the impact of thermal treatment. The coating process is conducted at elevated temperatures, and the effect of thermal treatment and the temperature-dependent properties of WC-Co have been thoroughly examined in numerous studies [34,35]. Thermal treatment has been shown to decrease the overall grain size and stabilize the fcc phase. However, the underlying causes of this behavior in the LMS context remain uncertain and are subject to further investigation.

5. Summary

In this study, we investigated the properties of cobalt in tungsten carbide tools, with cobalt serving as a binder phase, and its role in diamond coating adhesion. The study's foundation was the magnetic saturation values of several batches. The investigation proceeded with an analysis of the hexagonal close-packed (hcp) to face-centered cubic (fcc) ratio of cobalt in uncoated WC-Co samples. This analysis indicated the material's magnetic saturation behavior. A study of the X-ray diffraction (XRD) patterns of various WC-Co powders revealed negligible variation, indicating that the potential for magnetic deviation may occur during the manufacturing process. The following text is intended to provide a comprehensive overview of the subject matter.

We proceeded to investigate the impact of magnetic properties on cobalt utilizing Energy-Dispersive X-ray Spectroscopy (EDX) in Transmission Electron Microscopy (TEM). This analysis revealed the manner in which the magnetism of cobalt affects the dissolution of tungsten in the binder phase. Furthermore, the impact of magnetism on the lattice parameters of cobalt was confirmed.

The study also investigated the magnetic saturation WC-Co pre-treatment process, particularly the formation of a cobalt depletion layer through etching. This intermediate layer plays a pivotal role in ensuring the durability of diamond coating adhesion, as it serves as the bonding interface. Finally, the characterization of the diamond coating using Raman spectroscopy and TEM with Electron Energy Loss Spectroscopy (EELS) allowed for the assessment of the carbon hybridization within the coating. This characterization revealed partially carbon-filled voids, identified the distribution of sp^3 and sp^2 bonding, and provided insights into the coating's structure at the atomic level. Notwithstanding, the rHCP had been previously investigated both before and after the coating, resulting in a decrease for HMS samples and an increase for LMS samples. The effect on HMS can be explained by temperature-dependent properties; however, for NMS, the reason for this behavior remains unclear and requires further investigation. We showcased that high magnetic saturation (HMS) samples, which have less tungsten dissolved in the cobalt binder, were prone to excessive etching during pre-treatment. Tungsten stabilizes the cobalt binder, making it more noble and corrosion-resistant. Without sufficient tungsten, the cobalt is less stable and corrodes excessively. This excessive etching creates a deep and unstable depletion zone with a "crumbling edge." In this brittle, highly-etched state, the tungsten carbide (WC) grains can crumble and fracture. The resulting surface is a poor foundation for consistent carbon nucleation and growth.

The core-objective of this research was to attain a more profound comprehension of the influence of cobalt on layer adhesion, thereby providing avenues for the enhancement of WC-Co work tools' performance in wear-resistant industrial applications. The influence of the cobalt binder's magnetic properties, the formation of the cobalt

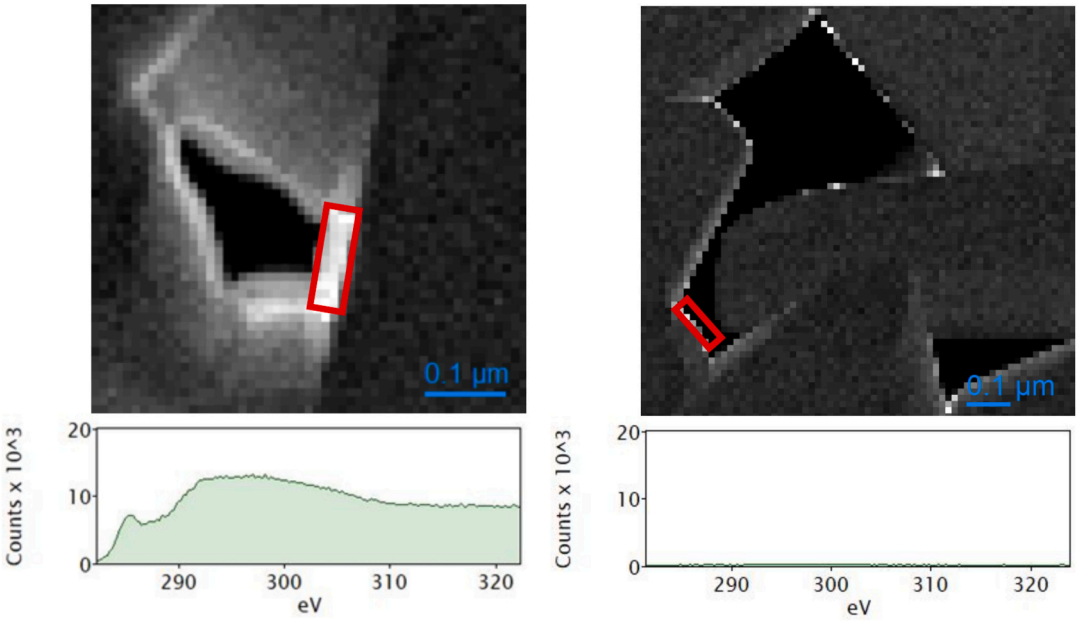

Fig. 22. STEM-EELS images of depleted cobalt pores with ELNES signal between 285 and 305. These images show the carbon present in the cobalt depleted pores (top row) of LMS (left, sample: 7472B_3) and HMS (right, sample: N7390B_4) samples, and the corresponding C-K ELNES signal (bottom row) of marked regions in red rectangles, for energies between 285 and 305 eV. (For interpretation of the references to colour in this figure legend, the reader is referred to the web version of this article.)

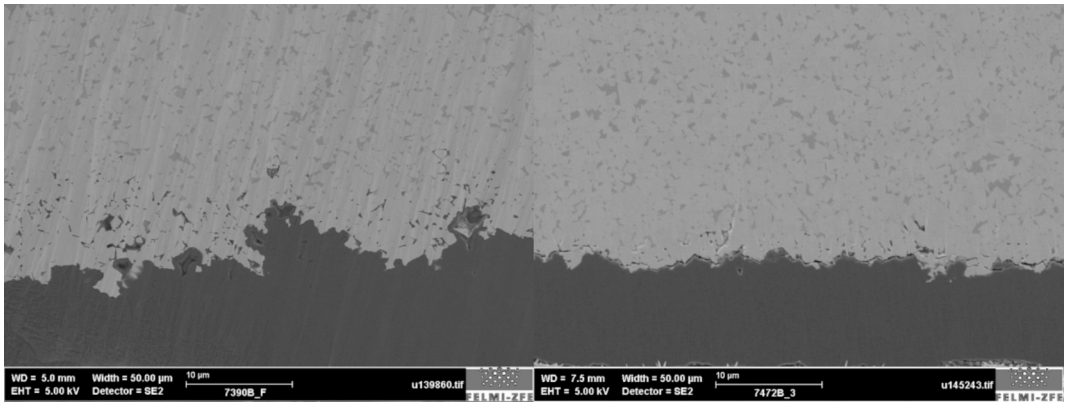

Fig. 23. SEM images of a cross section surface of coated WC-Co edge of an HMS (Left, sample: 7390B_F) and an LMS (right, LMS sample: 7472B_3), imaged using SE in SEM. Images show the surface morphology after coating.

depletion layer, and the carbon hybridization in the diamond coating on the adhesion and performance of WC-Co is demonstrated. It is imperative to emphasize that this issue pertained to the material itself rather than to the coating. For a diamond coating to adhere properly, cobalt must be etched from the outermost layers (interface) to allow diamond to nucleate and form. Diamond particles were seeded after etching to act as growth centers. The excessive etching of HMS samples, however, leaves a brittle, fractured surface with a large, unstable depletion zone. This prevents the diamond seeds from properly diffusing into the pores and forming nucleation zones. Instead of forming a well-ordered carbon structure, the carbon grows as amorphous carbon, which is more brittle than graphite. This is supported by Raman spectroscopy results, which show that HMS samples have a preference for amorphous carbon (broad G-band), whereas low magnetic saturation (LMS) samples, with a shallower and more stable depletion zone, favor a more crystalline graphite structure (sharp G-band). Thus, it was concluded that the poor adhesion in HMS samples is a result of the brittle, unstable depletion zone, which is a consequence of the material's magnetic saturation and its effect on the etching process. We recommend manufacturers of diamond coated WC-Co, specifically vanadium-doped, to either implement strict magnetic saturation criteria or sort the batches based on their BRM values. After sorting, the pretreatment recipe must be adapted to the BRM value, and take into consideration the cobalt content, to avoid material related failure.

CRediT authorship contribution statement

A. Alatrash: Writing – review & editing, Writing – original draft, Visualization, Validation, Methodology, Investigation, Formal analysis, Data curation, Conceptualization. **D. Steinmüller-Nethl:** Writing – review & editing, Validation, Supervision, Resources. **H. Fitzek:** Writing – review & editing, Validation, Investigation, Formal analysis. **S. Mitsche:** Writing – review & editing, Supervision. **D. Knez:** Investigation, Data curation. **M. Oberaigner:** Data curation. **J. Arnold:** Formal analysis. **A. Eckert:** Writing – review & editing, Validation, Resources. **W. Grogger:** Validation, Supervision, Funding acquisition.

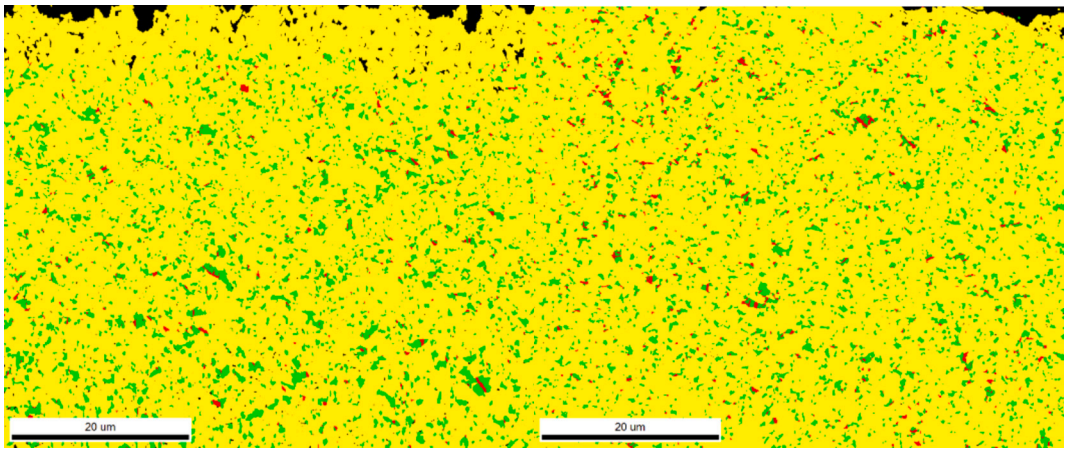

Fig. 24. Images of phase maps generated using EBSD of coated samples. Left: HMS sample (7390B_F), right: LMS sample (7472B_3). Colour code: red: hcp Cobalt; green: fcc Cobalt; yellow: Tungsten Carbide; black: no signal. Scans were done at the edge of the samples. (For interpretation of the references to colour in this figure legend, the reader is referred to the web version of this article.)

Table 7
rHCP of coated samples and corresponding BRM.

Batch No.	Sample No.	BRM (%)	rHCP (%)	Batch No.	Sample No.	BRM (%)	rHCP (%)
N7390B	2	97.2	13.0	7472B	2	80.7	3.42
N7390B	4	98	9.72	7472B	3	81.6	3.03
B7390B	2	96.4	14.0	6915 V	B	83.6	2.97
7390 V	E	94.5	7.39	6915B	C	83.6	2.88
7390B	F	94.5	7.48	0348B	14	88.28	1.78
8377B	2	84.9	3.20	1439 V	49	79.1	2.18
8377B	3	84.9	4.30	1439B	1	83.2	1.98

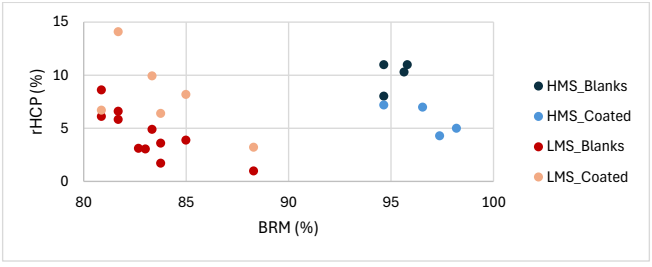

Fig. 25. Results of EBSD data showing rHCP for blanks and coated samples.

Author agreement statement

We the undersigned declare that this manuscript is original, has not been published before and is currently not being considered for publication elsewhere. We confirm that the manuscript has been read and approved by all named authors and that there are no other persons who satisfied the criteria for authorship but are not listed. We further confirm that the order of authors listed in the manuscript has been approved by all of us. We understand that the Corresponding Author is the sole contact for the Editorial process. He/she is responsible for communicating with the other authors about progress, submissions of revisions and final approval of proofs.

Funding source

This project has received funding from the Austrian Research Promotion Agency (FFG) (project "QualiTool", number 39177565). The funding agency took no role in the research.

Declaration of competing interest

The authors declare the following financial interests/personal relationships which may be considered as potential competing interests:

Anas Alatrash reports financial support was provided by Austrian Centre fo Electron Microscopy and Nanoanalysis. Anas Alatrash reports a relationship with Austrian Centre fo Electron Microscopy and Nanoanalysis that includes: employment. If there are other authors, they declare that they have no known competing financial interests or personal relationships that could have appeared to influence the work reported in this paper.

Acknowledgement

We thank Martina Dienstleder, Anita Rossmann-Perner, Arnela Blažević and Emma Kramer for their assistance in sample preparation. This project has received funding from the Austrian Research Promotion Agency (FFG) (project "QualiTool", number 39177565).

Data availability

Data will be made available on request.

References

[1] E. Lassner, W.-D. Schubert, Tungsten: Properties, Chemistry, Technology of the Element, Alloys, and Chemical Compounds, Springer Science & Business Media, 2012.
[2] O.-D. Jucan, R.-V. Gadalean, H.-F. Chicinas, N. Balc, C.-O. Popa, The assessment of the transversal rupture strength (TRS) and hardness of WC-Co specimens made via additive manufacturing and sinter-HIP, Metals 13 (6) (2023) 1051.
[3] B. Roebuck, E. Almond, A. Cottenden, The influence of composition, phase transformation and varying the relative F.C.C. and H.C.P. Phase contents on the properties of dilute Co-W-C alloys, Mater. Sci. Eng. 66 (2) (1984) 179–194.
[4] F. Kong, W. Zhao, H. Li, N. He, Effect of grain size and cobalt content on machining performance during milling tungsten carbide with PCD tool, Int. J. Refract. Met. Hard Mater. 123 (2024) 106780.
[5] B. Roebuck, P. Klose, K. Mingard, Hardness of hexagonal tungsten carbide crystals as a function of orientation, Acta Mater. 60 (17) (2012) 6131–6143.
[6] A. Tahir, G.-R. Li, M.-J. Liu, G.-J. Yang, C.-X. Li, Y.-Y. Wang, C.-J. Li, Improving WC-Co coating adhesive strength on rough substrate: finite element modeling and experiment, J. Mater. Sci. Technol. 37 (2020) 1–8.
[7] E. Ashkinazi, S. Fedorov, A. Khomich, V. Rogalin, A. Bolshakov, D. Sovyk, S. Grigoriev, V. Konov, Technology features of diamond coating deposition on a carbide tool, J. Carbon Res. 8 (77) (2022).
[8] W. Böhlke, Hartmetall, ein moderner Hochleistungswerkstoff, Mater. Werkst. (2002) 575–580.
[9] B. Kaplan, S. Norgren, M. Schwind, M. Selleby, Thermodynamic calculations and experimental verification in the WC–Co–Cr cemented carbide system, Int. J. Refract. Met. Hard Mater. 45 (2015) 257–262.

[10] V. Lamelas, M. Bonvalet Rolland, L. Toller-Nordstrom, R. de Oro Calderon, M. Walbruhl, A. Borgenstam, Broadening of the carbon window and the appearance of core-rim carbides in WC-Fe/Ni cemented carbides, J. Alloys Compd. 999 (2025) 175–178, 2924.
[11] J. Garcia, W. Strelsky, Process development and scale up of cementedcarbide production, in: Scale-up in Metallurgy, Verlag ProcessEng Engineering GmbH, 2010.
[12] I. Konyashin, S. Hlawatschek, B. Ries, F. Lachmann, F. Dorn, A. Sologubenko, T. Weirich, On the mechanism of WC coarsening in WC–co hardmetals with various carbon contents, Int. J. Refract. Met. Hard Mater. 27 (2) (2009) 234–243.
[13] J.M. Marshall, M. Giraudel, The role of tungsten in the Co binder: effects on WC grain size and hcp–fcc Co in the binder phase, Int. J. Refract. Met. Hard Mater. 49 (2015) 57–66.
[14] B. Winiarski, A. Gholinia, K. Mingard, M. Gee, G.E. Thompson, P.J. Withers, Broad ion beam serial section tomography, Ultramicroscopy 172 (2017) 52–64.
[15] A. Alatrash, D. Steinmüller-Nethl, S. Mitsche, A. Eckert, W. Grogger, Microstructural alternations in tungsten carbide, Pract. Metallogr. 64 (2025) 4.
[16] J. Garcia, V.C. Cipres, A. Blomqvist, B. Kaplan, Cemented carbide microstructures: a review, Int. J. Refract. Met. Hard Mater. 80 (2019) 40–68.
[17] P. Rugóczky, G. Muránszky, J. Lakatos, Comparative investigations of the selective co, IOP Conf. Ser. Mater. Sci. Eng. 613 (012015) (2019).
[18] G. Desbois, J.L. Urai, J.H. de Bresser, Fluid distribution in grain boundaries of natural fine-grained rock salt deformed at low shear stress: implications for rheology and transport properties, J. Struct. Geol. 43 (2012) 128–143.
[19] B. Schönhuber, Measurement of Residual Stress in Cemented Carbide sUsing Electron Backscatter Diffraction, Graz University of Technology, Graz, 2020.
[20] H. Suzuki, T. Yamamoto, Effects of carbon content on some properties of WC-10% (Co-Ni) cemented carbides, J. Jpn. Soc. Powder Powder Metall. 15 (2) (1968–1969) 68–71.
[21] R. Khmyrov, A. Shevchukov, A. Gusarov, T. Tarasova, Phase composition and microstructure of WC–co alloys obtained by selective laser melting, Mech. Ind. 18 (2017).
[22] S. Hochstrasser-Kurz, Y. Mueller, C. Latkoczy, S. Virtanen, P. Schmutz, Analytical characterization of the corrosion mechanisms of WC-co by electrochemical methods and inductively-coupled plasma mass spectroscopy, Corros. Sci. 49 (2007) 2002–2020.
[23] R. Haubner, W. Kalss, Diamond deposition on hardmetal substrates – comparison of substrate pre-treatments and industrial applications, Int. J. Refract. Met. Hard Mater. 28 (4) (2010) 475–483.
[24] D. Long, The Raman Effect: A Unified Treatment of the Theory of Raman Scattering by Molecules, Wiley & Sons Ltd, 2002.
[25] R. Yuan, Y. Guo, I. Gurgan, N. Siddique, Y.S. Li, S.N. Jang, S.H. Kim, Raman spectroscopy analysis of disordered and amorphous carbon materials: a review of empirical correlations, Carbon 238 (120214) (2025).
[26] E.H. Hasdeo, A.R.T. Nugraha, M.S. Dresselhaus, R. Saito, Breit-Wigner-Fano line shapes in Raman spectra of graphene, Phys. Rev. B 90 (24) (2014) 245140.
[27] J.R. Ferraro, K. Nakamoto, C.W. Brown, Introductory Raman Spectroscopy, Academic Press, 2003.
[28] C. Bommier, D. Mitlin, X. Ji, Internal structure – Na storage mechanisms – electrochemical performance relations in carbons, Prog. Mater. Sci. 97 (2018) 170–203.
[29] F. Hofer, B. Luo, Towards a practical method for EELS quantification, Ultramicroscopy 38 (2) (1991) 159–167.
[30] V.J. Keast, Application of EELS in materials science, Mater. Charact. 73 (2012) 1–7.
[31] L. Garvie, A. Carven, R. Brydson, Use of electron-energy loss near-edge fine structure in the study of minerals, Am. Mineral. 79 (1994) 411–425.
[32] I. Dörfel, H. Rooch, W. Österle, Microstructural features of CVD diamond coatings on WC-Co – a TEM, in: EMC2012, 2012.
[33] X. Wang, Y. Jinwen, Interface characteristics of CVD diamond coating on WC-co cemented carbide substrate, Surf. Coat. Technol. 485 (130886) (2025).
[34] Z. Xiang, Z. Li, F. Chang, P. Dai, Effect of heat treatment on the microstructure and properties of ultrafine WC–Co cemented carbide, metals 9 (12) (2019).
[35] B. Roebuck, Temperature dependent properties of Co-W-C alloys, Int. J. Refract. Met. Hard Mater. 111 (106073) (2023).